Fast and Cost-Effective Three-Dimensional Microwave Imaging Using a Cylindrical Setup

Reza K. Amineh

Department of Electrical and Computer Engineering
New York Institute of Technology
New York, USA
rkhalaja@nvit.edu

Abstract—In this paper, we propose a fast and low-cost cylindrical microwave imaging system based on the use of arrays of transmitter and receiver antennas and a customized low-cost data acquisition circuit using off-the-shelf components. The complex-valued scattered data captured with the proposed system is processed using near-field holographic image reconstruction. To enhance this technique, standardized minimum norm (SMN) approach is employed to solve the relevant systems of equations. The performance of the proposed imaging technique and the data acquisition system is demonstrated via simulations and experiments.

Keywords—antenna arrays, holography, microwave imaging, standardized minimum norm.

I. Introduction

Microwave imaging has been employed in various applications such as concealed weapon detection (e.g., see [1]), non-destructive testing (e.g., see [2]), biomedical imaging (e.g., see [3]), etc. One mature and robust application is millimeter wave security screening of the passengers at the airports (e.g., see [4]) which is based on the holographic techniques. These techniques have also been extended to the applications such as biomedical imaging and non-destructive testing where the imaged object is in the near-field of the antennas (e.g., see [5]). In near-field holographic imaging, the complex-valued data can be acquired over rectangular or cylindrical apertures [5].

Conventionally, in holographic imaging, wideband data is required to reconstruct three-dimensional (3D) images (e.g., see [4], [5]). However, in [6], an approach has been presented to implement 3D imaging using data collected over the narrowest possible band and the use of an array of receiver antennas. This allowed the use of a compact and low-cost data acquisition system along with resonant antennas which increase the dynamic range of the imaging system. Although the proposed system in [6] is more affordable for various industrial settings compared to vector network analysers (VNAs), it is still slow due to the mechanical scanning of a cylindrical aperture.

In this paper, a cylindrical near-field microwave holographic imaging system is proposed based on the use of the transceiver system in [6] and arrays of transmitter and receiver antennas to expedite the data acquisition process. The validity of the proposed imaging technique is demonstrated via simulation and experimental examples.

This project has been supported by US national science foundation (NSF), award No. 1920098, and New York Institute of Technology's (NYIT) Institutional Support for Research and Creativity (ISRC) Grants.

Maryam Ravan

Department of Electrical and Computer Engineering
New York Institute of Technology
New York, USA
mravan@nvit.edu

II. THEORY

Here, we first review the theory of near-field holographic imaging when using arrays of transmitter and receiver antennas along the azimuthal direction and then propose the use of standardized minimum norm (SMN) approach to improve the image reconstruction process.

A. Near-Field Holographic Imaging with Antenna Arrays

Fig. 1(a) illustrates the proposed cylindrical microwave imaging system with the antenna arrays. Fig. 1(b) shows the top view of the setup. N_T transmitter and N_R receiver antennas are distributed along the azimuthal axis ($N_A = N_R + N_T$ antennas uniformly cover a full circle). This antenna array scans a cylindrical aperture with radius of r_A and height of z_A by collecting the data electronically along the azimuthal direction and mechnically along the longitudinal direction (at multiple heights z_I , $I = 1, ..., N_T$ uniformly coversing the span of z_A) at

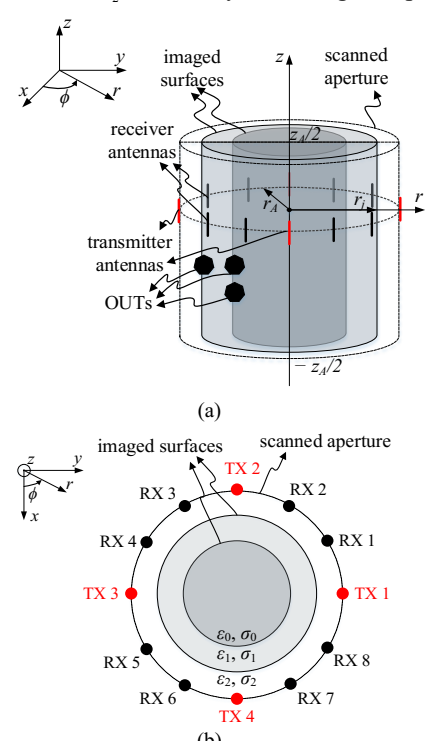


Fig. 1. (a) The proposed cylindrical imaging setup and (b) top view of the setup $(\epsilon_j$ and $\sigma_j, j=0,...,N_r$ denote the electrical permittivity and conductivity of the media, respectively). TX and RX stand for transmitter and receiver antennas, respectively.

frequencies ω_{n_f} , $n_f=1,...,N_f$. Electronic scanning is performed such that at each z_l , one transmitter at a time, illuminates the objects under test (OUTs) while all the receivers collect the scattered data.

In near-field holographic imaging, the imaging system is assumed to be linear and space invariant (LSI). First, the point-spread functions (PSFs) of the imaging system $E_{j,a_m}^{SC,CO}(\phi_{k'},z_l,\omega_{n_f})$ are recorded by placing small calibration objects (COs), one at a time, at $(r_j,0,0)$, $j=1,\ldots,N_r$ positions, where N_r is the number of the imaged cylindrical surfaces, a_m is the number of the transmitter, and $\phi_{k'}$, $k'=1,\ldots,N_R$, is the azimuthal angle of the receiver antenna. Then, the complex-valued scattered fields $E_{a_m}^{SC}(\phi_{k'},z_l,\omega_{n_f})$ for the OUTs are recorded. To obtain responses at uniformly distributed angular positions ϕ_k , $k=1,\ldots,N_A$, at each height z_l , interpolation is applied on the responses.

In near-field holographic imaging technique [5], the interpolated scattered field $E^{SC}_{a_m}(\phi_k,z_l,\omega_{n_t})$ can be written as:

$$E_{a_m}^{SC}(\phi_k, z_l, \omega_{n_f}) = \sum_{j=1}^{N_r} E_{j, a_m}^{SC, CO}(\phi_k, z_l, \omega_{n_f}) *_{\phi} *_{z} f_{j}(\phi_k, z_l)$$
 (1)

where $*_{\phi}$ and $*_{z}$ denote the convolutions along the ϕ and z directions, respectively, and $f_{j}(\phi_{k},z_{l})$ is the contrast function of the OUTs. By writing (1) at all frequencies and for all transmitters and then applying discrete-time Fourier Transform (DTFT) and discrete Fourier Transform (DFT) to both sides of the equations along z and ϕ directions, respectively, the following system of equations is obtained at each spatial frequency pair:

$$\tilde{\tilde{\mathbf{E}}}^{SC} = \tilde{\tilde{\mathbf{D}}}\tilde{\tilde{\mathbf{F}}}, \qquad (2)$$

where

$$\underline{\underline{\tilde{\mathbf{E}}}}^{SC} = \begin{bmatrix} \underline{\tilde{\mathbf{E}}}_{1}^{SC} \\ \vdots \\ \underline{\tilde{\mathbf{E}}}_{N_{T}}^{SC} \end{bmatrix}, \ \underline{\underline{\tilde{\mathbf{D}}}} = \begin{bmatrix} \underline{\tilde{\mathbf{D}}}_{1} \\ \vdots \\ \underline{\tilde{\mathbf{D}}}_{N_{T}} \end{bmatrix}, \ \underline{\tilde{\mathbf{E}}} = \begin{bmatrix} \tilde{\mathbf{f}}_{1}(\boldsymbol{\kappa}) \\ \vdots \\ \tilde{\mathbf{f}}_{N_{r}}(\boldsymbol{\kappa}) \end{bmatrix},$$
(3)

and

$$\tilde{\underline{\underline{\tilde{E}}}}_{a_m}^{SC} = \begin{bmatrix}
\tilde{\underline{\tilde{E}}}_{a_m}^{SC}(\boldsymbol{\kappa}, \omega_1) \\
\vdots \\
\tilde{\underline{\tilde{E}}}_{a_m}^{SC}(\boldsymbol{\kappa}, \omega_{N_f})
\end{bmatrix},$$
(4)

$$\tilde{\underline{\mathbf{D}}}_{a_m} = \begin{bmatrix}
\tilde{\mathbf{E}}_{1,a_m}^{SC,CO}(\boldsymbol{\kappa},\omega_1) & \cdots & \tilde{\mathbf{E}}_{N_r,a_m}^{SC,CO}(\boldsymbol{\kappa},\omega_1) \\
\vdots & \ddots & \vdots \\
\tilde{\mathbf{E}}_{1,a_m}^{SC,CO}(\boldsymbol{\kappa},\omega_{N_f}) & \cdots & \tilde{\mathbf{E}}_{N_r,a_m}^{SC,CO}(\boldsymbol{\kappa},\omega_{N_f})
\end{bmatrix}, (5)$$

$$\begin{split} &\tilde{\tilde{\mathbf{E}}}_{a_m}^{SC}(\boldsymbol{\kappa},\omega_{n_f}) \;,\;\; \tilde{\tilde{\mathbf{E}}}_{j,a_m}^{SC,CO}(\boldsymbol{\kappa},\omega_{n_f}) \;,\; \text{and} \;\; \tilde{\tilde{\mathbf{f}}}_{j}(\boldsymbol{\kappa}) \;\; \text{are functions after} \\ &\text{taking DFT along} \;\; \boldsymbol{\phi} \;\; \text{axis and DTFT along} \;\; \boldsymbol{z} \;\; \text{axis of} \\ &E_{a_m}^{SC}(\boldsymbol{\phi}_k,z_l,\omega_{n_f}) \;\;,\;\; E_{j,a_m}^{SC,CO}(\boldsymbol{\phi}_k,z_l,\omega_{n_f}) \;\;,\;\; \text{and} \;\;\; \boldsymbol{f}_{j}(\boldsymbol{\phi}_k,z_l) \;\;, \end{split}$$

respectively, and $\kappa = (k_{\phi}, k_z)$ where k_{ϕ} and k_z are Fourier variables corresponding to k and l, respectively.

The system of equations in (2) is conventionally solved using minimum norm (MN) approach ([5], [6]) to obtain the values of $\tilde{\mathbf{f}}_j(\mathbf{k})$, $j=1,\ldots,N_r$. Then, inverse DTFT along z and inverse DFT along ϕ are applied to reconstruct images $f_j(\phi_k,z_l)$ over all imaged surfaces. At the end, the normalized modulus of $f_j(\phi_k,z_l)$, $|f_j(\phi_k,z_l)|/M$, where M is the maximum of $|f_j(\phi_k,z_l)|$ for all r_j , is plotted to obtain a 2D image of the OUTs at each surface. We call $|f_j(\phi_k,z_l)|/M$ the normalized image.

B. Applying Standardized Minimum Norm Approach

The common approach to solve the systems of equations in near-field holographic imaging is the well-known MN solution ([5][6]). As many real-world phenomena, scattering problems have the effect of low-pass filters in their forward model. Therefore, in solving the inverse scattering problem, the inverse mapping operates as a high-pass filter that has the undesirable tendency of amplifying noise. To alleviate this issue, regularization terms can be applied in the minimization problem. Here, inspired by standardized low-resolution brain electromagnetic tomography using EEG data [7], we apply SMN approach to solve the system of equations.

First, the cost function to be minimized is constructed as:

$$J = \left\| \underline{\tilde{\mathbf{E}}}^{SC} - \underline{\tilde{\mathbf{D}}}\underline{\tilde{\mathbf{F}}} \right\|^2 + \alpha \left\| \underline{\tilde{\mathbf{F}}} \right\|^2, \tag{8}$$

where $\|\cdot\|$ is the 2-norm operator and $\alpha \geq 0$ is a regularization parameter. This parameter is taken as the variance of the noise in the simulated or measured data. The functional J is to be minimized with respect to $\tilde{\underline{\mathbf{F}}}$, for given $\tilde{\underline{\mathbf{D}}}$, $\tilde{\underline{\mathbf{E}}}^{SC}$, and α . The explicit solution to this minimization problem is:

$$\frac{\hat{\tilde{\mathbf{E}}}}{\tilde{\mathbf{E}}} = P \tilde{\tilde{\mathbf{E}}}^{SC}, \qquad (9)$$

where

$$P = \underline{\underline{\tilde{\mathbf{p}}}}^{\mathsf{H}} \mathbf{L} \left[\mathbf{L} \underline{\underline{\tilde{\mathbf{p}}}} \underline{\underline{\tilde{\mathbf{p}}}}^{\mathsf{H}} \mathbf{L} + \alpha \mathbf{L} \right]^{+}, \qquad (10)$$

$$\begin{split} & \tilde{\tilde{\mathbf{F}}} \text{ is the estimate of } \tilde{\tilde{\mathbf{F}}} \text{ , } L_{N_{\varpi}N_{A}\times N_{\varpi}N_{A}} = I-11^{T} \ / 1^{T}1 \text{ denotes the centering matrix, } I_{N_{\varpi}N_{A}\times N_{\varpi}N_{A}} \text{ is the identity matrix, } 1_{N_{\varpi}N_{A}\times 1} \text{ is a vector of ones, } \left[\cdot \right]^{H} \text{ is Hermitian transpose operation, and } \left[\cdot \right]^{+} \text{ denotes Moore-Penrose pseudoinverse. Standardization of the estimate } \tilde{\tilde{\mathbf{F}}} \text{ requires an estimate of its variance. The true variance of } \tilde{\tilde{\mathbf{F}}} \text{ is equal to the identity matrix but this is for an ideal case when } \tilde{\tilde{\mathbf{F}}} \text{ is estimated without error. In practice, variance of } \tilde{\tilde{\mathbf{F}}} \text{ denoted by } S_{\tilde{\mathbf{F}}} \text{ can be obtained as [7]:} \end{split}$$

$$S_{\frac{\tilde{E}}{\tilde{E}}} = P\left(\tilde{\underline{\underline{\tilde{p}}}}\tilde{\underline{\underline{\tilde{p}}}}^{H} + \alpha L\right)P^{H} = \tilde{\underline{\underline{\tilde{p}}}}^{H}\left(\tilde{\underline{\underline{\tilde{p}}}}\tilde{\underline{\underline{\tilde{p}}}}^{H} + \alpha L\right)^{+}\tilde{\underline{\underline{\tilde{p}}}}.$$
 (11)

The standardization of $\hat{\tilde{\mathbf{F}}}$ is then estimated as [8]:

the process described in Section II.A.

$$\frac{\hat{\mathbf{E}}}{\mathbf{F}} = \sqrt{(\text{Diag}(\mathbf{S}_{\hat{\mathbf{F}}}))^{-1}} \mathbf{P} \mathbf{E}^{\mathbf{E}SC}, \qquad (12)$$

where $\text{Diag}(S_{\underline{\hat{\tilde{E}}}})$ is the diagonal matrix formed by the diagonal elements of $S_{\underline{\hat{\tilde{E}}}}$. Having $\widehat{\underline{\tilde{\tilde{E}}}}$, the image formation is similar to

III. SIMULATION RESULTS

First, we assess the performance of the proposed imaging technique via FEKO simulations. The study is performed by simulating responses at 5 frequencies within a band of 0.4 GHz around center frequency of 1.7 GHz. To have a realistic study of the performance of the imaging technique, White Gaussian noise is added to the simulated data with signal-to-noise ratio (SNR) of 20 dB. Besides, to assess the quality of the

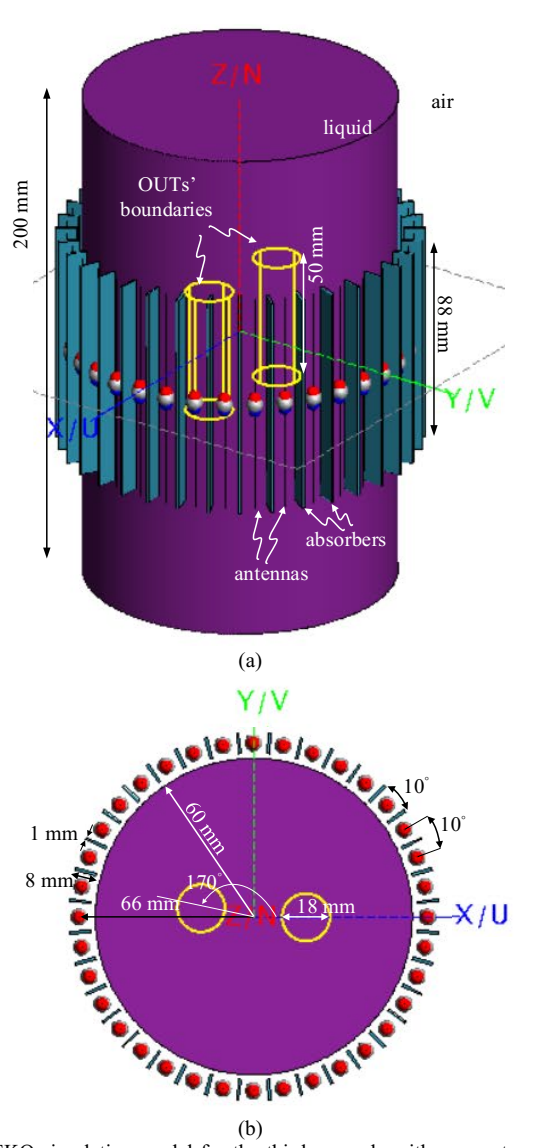


Fig. 2. FEKO simulation model for the third example with parameter values similar to the measurement setup: (a) isometric view and (b) top view.

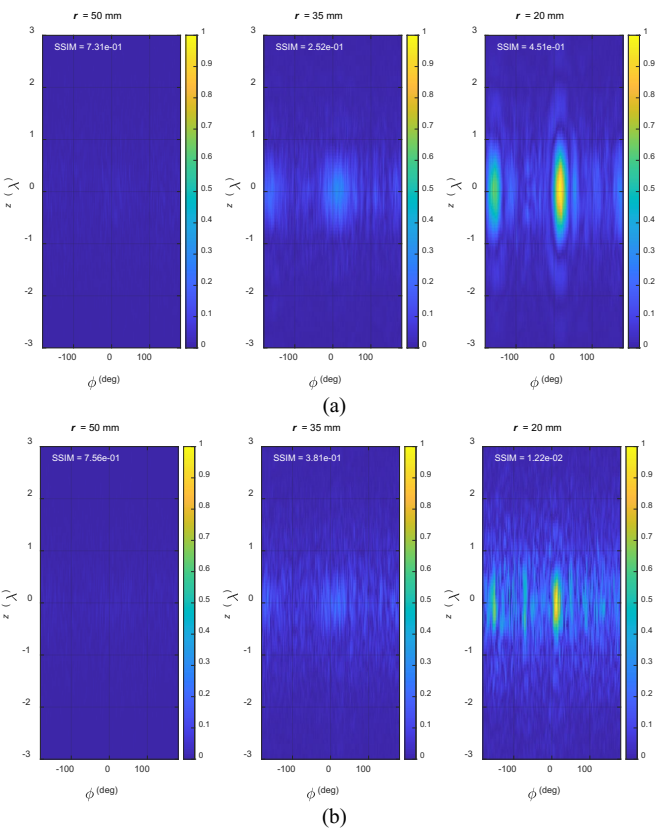


Fig. 3. Normalized images for the simulation example: (a) with microwave absorbers and (b) without microwave absorbers.

reconstructed images, we employ the structural similarity (SSIM) index [9]. Here, SSIM is computed for each reconstructed 2D image when taking the true OUTs' image as the reference. The true image has a value of 1 at the pixels overlapping the OUTs and 0 elsewhere. Higher SSIM values indicate higher similarity to the true image.

The simulation setup is similar to the one used later in the experiments. Fig. 2 shows this setup, in which, a cylindrical host medium has properties of $\varepsilon_r = 22$ and $\sigma = 1.25$ S/m. The antennas are resonant dipoles at 1.7 GHz and surround this medium in the air. To reduce the coupling between the antennas, microwave absorbing sheets (absorbers) made of carbon fibers with properties of $\varepsilon_r = 4.54$ and $\sigma = 55000$ S/m are placed in between the antennas. The angular separation between transmitter and adjacent receiver antennas are $\Delta \phi_T = 40^{\circ}$ and $\Delta \phi_R = 10^{\circ}$, respectively (no receiver antennas at the position of transmitters). This indicates that there are 9 transmitter antennas and 27 receiver antennas. The synthesized aperture has a length of 150 mm and 21 samples along the z axis. The hidden objects are two PEC cylinders with diameter of 18 mm and height of 50 mm centered at cylindrical coordinates (r, ϕ, z) of (20 mm, 0°, 0) and (20 mm, -170°, 0) and aligned along the z axis. The cylindrical imaged surfaces are at r_i = 50 mm, 35 mm, and 20 mm. Thus, to collect PSF data, we place cylindrical PEC objects with diameter of 18 mm and height of 10 mm at cylindrical coordinates (r, ϕ, z) of $(r_i, 0, 0)$, one at a

time, and simulate the responses.

Fig. 3(a) shows the reconstructed images for this example. It is observed that the two hidden objects can be reconstructed well. The coupling between two adjacent antennas is almost -6 dB and -14 dB without and with the use of microwave absorbers, respectively. To study the effect of using microwave absorbers, we perform imaging for the same setup but without microwave absorbers. Fig. 3(b) shows the images for this case. It is clear that the quality of the reconstructed image of the OUTs is lower compared to that in Fig. 3(a).

IV. EXPERIMENTAL RESULTS

Here, we present the design of a low-coast and fast imaging system operating at 1.6-1.8 GHz. Fig. 4 shows the imaging system with its main components. The data acquisition system consists of microwave circuits to transmit and receive signals, arrays of transmitter and receiver antennas, two switching networks for selecting the antennas, and the scanning system. The antennas are placed inside a customized holder made by 3D printing. Microwave absorbing sheets are placed in slots between the antennas to reduce their direct coupling. A container with diameter of 120 mm and height of 200 mm is filled with a mixture of water and glycerin with properties of $\varepsilon_r = 22$ and $\sigma = 1.25$ S/m within the operating frequency band. The OUTs are plastic cylinders with diameter of 18 mm and height of 50 mm covered by thin copper sheets. The details of the transceiver system can be found in [6]. Two separate switching networks are built for transmitter and receiver antenna arrays using EV1HMC321ALP4E modules which are RF SP8T switches from Analog Devices. Here, the antenna arrays consist of 36 antennas: 9 transmitters and 27 receivers. uniformly distributed along ϕ , similar to the simulation setup. We use mini GSM/Cellular Quad-Band antennas from Adafruit Company. The angular separation between transmitters and adjacent receivers are 40° and 10°, respectively.

Two OUTs are placed at cylindrical coordinates (r, ϕ, z) of (20 mm, -170° , 0) and (20 mm, 0° , 0). The container with OUTs is scanned along z while the antenna arrays are stationary. Scanning along z is performed from -2λ to 2λ with 21 sampling steps, where λ is the wavelength at the center frequency of 1.7 GHz for the used mixture.

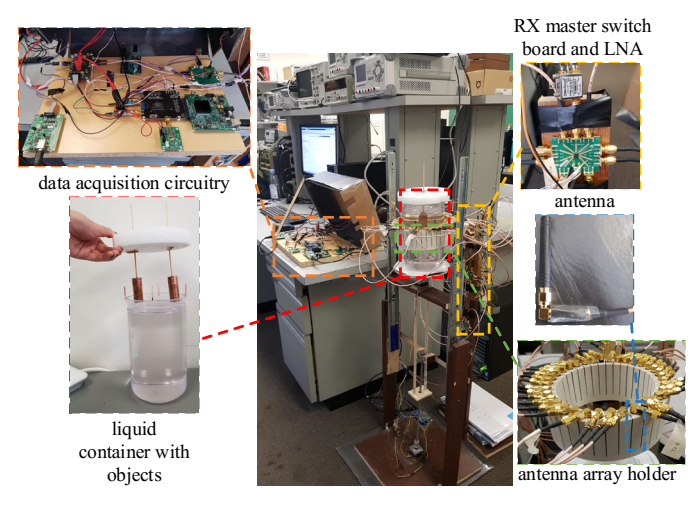


Fig. 4. Imaging system with its main components zoomed in.

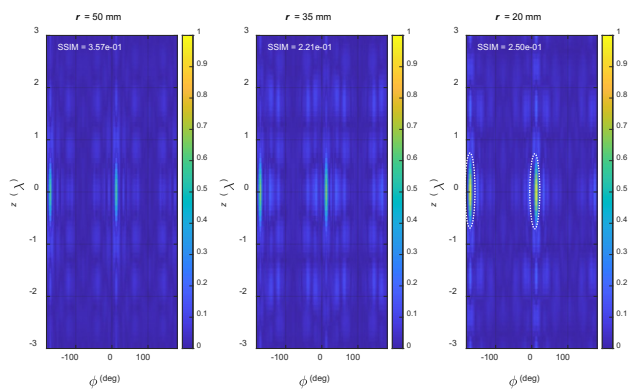


Fig. 5. Normalized images for two OUTs placed on the inner surface. White dotted lines show the true positions of the objects.

The complex-valued response for each receiver is constructed from I and Q channels of the quadrature receiver unit. A calibration process is performed to reduce the effects of background medium, air-mixture boundaries, and slight differences between the antennas. After collecting the PSFs and OUT responses and implementing the calibration process, the image reconstruction method is applied. Fig. 5 shows the reconstructed images It is observed that the objects can be reconstructed well.

V. CONCLUSION

In this paper, a low-cost and fast 3D microwave imaging system was proposed using a customized transceiver circuit and antenna arrays. The use of antenna arrays allows for fast data acquisition along the azimuthal direction. High quality of the reconstructed images was achieved by applying near-field holographic imaging with SMN approach to solve the relevant system of equations at each spatial frequency variable pair. The proposed imaging technique can be employed in various applications and in various industrial settings where the cost and speed are important factors.

REFERENCES

- M. C. Kemp, "Millimetre wave and terahertz technology for the detection of concealed threats - a review," *Proc. of SPIE*, vol. 6402, 2006.
- [2] R. Zoughi, Microwave Non-Destructive Testing and Evaluation. Kluwer Academic Publishers, 2000.
- [3] N. K. Nikolova, "Microwave near-field imaging of human tissue and its applications to breast cancer detection," *IEEE Microwave Mag.*, vol. 12, no. 7, pp. 78–94, Dec. 2011.
- [4] D. M. Sheen, D. L. McMakin, and T. E. Hall, "Three-dimensional millimeter-wave imaging for concealed weapon detection," *IEEE Transactions on Microwave Theory and Techniques*, vol. 49, no. 9, pp. 1581–1592, Sep. 2001.
- [5] R. K. Amineh, N. K. Nikolova, and M. Ravan, Real-Time Three-Dimensional Imaging of Dielectric Bodies Using Microwave/Millimeter Wave Holography. Wiley & IEEE Press, ISBN: 978-1-119-53886-8, 2019.
- [6] H. Wu and R. K. Amineh, "A low-cost and compact three-dimensional microwave holographic imaging system," *Electronics*, vol. 8, no. 9, 2019.
- [7] R. D. Pascual-Marqui, "Standardized low resolution brain electromagnetic tomography (sLORETA): Technical details," *Methods Find. Exp. Clin. Pharmacol.*, vol. 24, suppl D:5-12, pp. 1–16, 2002.
- [8] A. M. Dale, A. K. Liu, B. R. Fischl, R. L. Buckner, J. W. Belliveau, J. D. Lewine, and E. Halgren, "Dynamic statistical parametric mapping: combining fMRI and MEG for highresolution imaging of cortical activity," *Neuron*, vol. 26, pp. 55-67, 2000.
- [9] W. Zhou, A. C. Bovik, H. R. Sheikh, and E. P. Simoncelli, "Image quality assessment: from error visibility to structural similarity," *IEEE Trans. on Image Proc.*, vol. 13, no. 4, pp. 600–612, April 2004.